Specific core-shell approaches and related properties in nanostructured ferroelectric ceramics

Catherine Elissalde, Chung U-Chan, François Roulland, Romain Berthelot, Alla M. Artemenko, Jérôme Majimel, Sergey Basov, Luc Piraux, Bernard Nysten, Stéphane Mornet, et al.

"Specific core-shell approaches and related properties in nanostructured ferroelectric ceramics"

C. Elissalde[1], U.C. Chung[1], F. Roulland[2], R. Berthelot[3], A. Artemenko[1], J. Majimel[1], S. Basov[1,4], L. Piraux[4], B. Nysten[4], S. Mornet[1], C. Aymonier[1], C. Estournès[5] and M. Maglione[1]

[1]*ICMCB-CNRS, Université de Bordeaux, 87 Avenue du Docteur Schweitzer, 33600 Pessac, France*

[2]*IPCMS, Université de Strasbourg, 23 Rue du Loess, 67200 Strasbourg, France*

[3]*ICGM-CNRS, Université de Montpellier, 34095 Montpellier Cedex 5, France*

[4]*BSMA-IMCN, Université catholique de Louvain, 1 Place Croix du Sud, B-1348 Louvain-la-Neuve, Belgium*

[5] *CIRIMAT, Université de Toulouse, CNRS, Université Toulouse 3 - Paul Sabatier, 118 Route de Narbonne, 31062 Toulouse cedex 9 - France*.

Abstract

Interfaces are a major issue when designing ferroelectric nanostructured materials with tailored properties. In a context of integration and multifunctionality in the field of electronics, several strategies have been developed to control the microstructure and defect chemistry of interfaces that strongly impact the macroscopic properties. The suitability of the core-shell approaches that allow a subtle tuning of interface phenomena at different scales has been widely demonstrated. We focus here on the flexibility of the core-shell approach devoted to the processing of nanostructured ferroelectric composites. Our strategy relies on the use of advanced synthesis processes to design ferroelectric grains coated with shells of different nature, morphology and crystallinity. Typical examples will be reviewed with a specific attention on their impact on both microstructure and dielectric properties. Our approach, based also on the use of fast sintering technique, provides a guidance to design 3D bulk nanostructured ferroelectrics while controlling and/or exploiting size, interface and defects chemistry. The contribution of specific spectroscopies to probe interfacial chemistry and defects is underlined. The high density of interfaces in core-shell materials is obviously an advantage to target additional functionality such as magneto-electric coupling. This is illustrated in 3D composites and one dimensional nanostructures that coaxially combine electric and magnetic materials. The core-shell approach described here could be transferred to a much broader range of materials covering many functionalities provided a deeper understanding of the interfaces at the atomic scale is achieved and a further development of low temperature processing is reached.

1. Introduction

Thanks to their high permittivity and to its tunability, ferroelectric oxides are ideally suited for passive components in electronics such as capacitors, resonators, filters, piezoelectric transducers. Capacitors in particular, are essential in most of the electronic devices and share a large part of the mass market in the areas of information and communication technology and electronics. The current expectations are driven by the needs to deliver ever-greater levels of functionality within smaller devices, the available component space becoming increasingly constrained. The design of small components leads to a growing need for high specific capacity. Barium titanate, $BaTiO_3$, used as the reference material in the multilayer ceramic capacitor (MLCC) industry, is considered as one of the most important functional

materials. To extend its range of applications, it is desirable to control the permittivity value as well as its temperature and electric field dependences. In addition, to allow the integration into devices and to broaden the frequency range of use, dielectric losses have to be drastically decreased up to the GHz range. Such versatility in the dielectric characteristics can be reached in ferroelectric ceramics thanks to different strategies based on chemical substitutions, dopants, grain size, and multi-materials. Among these approaches, core-shell processing and modelling have been used for interface related phenomena in nanograins: inhomogeneity of spontaneous polarization from the surface to the grain core (size effects), local composition gradients (intrinsic point defects and chemical substitution), surface coating (nanostructured composites). The strong temperature dependence of the permittivity of $BaTiO_3$ (BT) based ceramics can be efficiently softened reducing the grain size down to about 100nm. In this size range, the core-shell structure consists of inner tetragonal core, gradient lattice strain layer, and surface cubic layer. The so-called size effects in ferroelectrics were significantly investigated during the last decades [1-4] and will not be detailed here. We will only briefly discuss the core-shell approach used to control the chemical inhomogeneity at the grain scale that also leads to ceramics exhibiting stable dielectric behavior over temperature [5].

We will focus on the core-shell approaches dedicated to the composite route that is particularly suitable not only to tailor the dielectric characteristics but also to generate new functionalities [6-9]. The major issue when designing tailor-made nanostructured ferroelectric materials is the control of the interfaces in a broad sense i.e. charged interfaces, grain boundaries, interphases between different components [10]. Through an overview of recent results, we will underline the progresses made in the synthesis of nanoscale-designed ferroelectric particles, ceramics and composites [6, 11]. In particular, promising wet chemical routes (seed growth process, thermolysis, supercritical fluid synthesis) to control stoichiometry, crystallinity, surface reactivity and functionalization will be emphasized. The suitability of Spark Plasma Sintering (SPS) to provide advanced nanostructured ceramics with tailored functionalities will be also demonstrated. Specific characterizations such as Electron Paramagnetic Resonance and the broadband dielectric spectroscopy (in the high-frequency range up to the infra-red) will be highlighted. Both techniques are particularly well suited to probe defect structure and interfaces in inhomogeneous materials exhibiting different bulk and grain boundary properties as well as in nanostructured ceramics with components of different dielectric properties [12-14]. Finally, illustrations of the core-shell approach to design multiferroic nanocomposites will be presented.

2. Chemical substitution and core-shell grains in fine-grained microstructures

Specific chemical core-shell microstructures were initially developed in the 80-90's in order to adjust $BaTiO_3$ based ceramic multilayer formulation to fit with the expectations of the so-called X7R components that require less than ±15% deviation from the 25 °C dielectric constant value over a temperature range of - 55 °C to 125 °C. The grain structure consists of two regions, a core made of pure barium titanate and a shell containing a non-uniform distribution of the dopants incorporated during

conventional densification process. The formation of core-shell microstructures requires a liquid phase sintering during which a subtle balance between thermodynamics and kinetics has to be reached to ensure chemical inhomogeneity. $BaTiO_3$ based ceramics with addition of ZrO_2 [15], LiF [16], Nb_2O_5 [17], MgO and rare earth oxides [18] were investigated reporting a variety of microstructures and tailored dielectric properties. The observed broadening of the dielectric constant peak as a function of temperature results from a distribution of local Curie temperature arising from the incorporation and non-uniform distribution of dopants within the shell. The broad phase transition in core-shell ceramics can be tuned not only by adjusting the nature and amount of additives but also by adjusting the sintering conditions. As a result a wide range of attractive properties for X7R capacitors applications can be obtained.

3. Nanoscale-designed ferroelectric particles and fast sintering process

Tailored microstructures for stable and enhanced dielectric properties have been largely developed at the nanoscale. Scaling effects in perovskite ferroelectrics are of main concern regarding applications including MLCC technology. The raising demand on increased volumetric capacitance and reduced operation voltage has led to a decrease of the dielectric layers thickness in MLCC from over 10 microns down to 100 nm and below during the past decade. As a result it is still a challenge to overcome the change in properties and the associated drawbacks arising from this downscaling. A complete review focused on the role of electrical and mechanical boundary conditions, grain size and thickness effects was recently proposed by J. F. Ihlefeld et al. [3]

Different strategies aiming the dielectric properties control at the nanoscale will be described in this section, most of them target interface and grain boundary engineering. Here the core-shell approach will be defined in terms of coating particles with materials of different nature or composition prior to the sintering step. Such a recent approach in the field of ferroelectrics has provided particularly original microstructures opening new pathways towards tailored functional and multifunctional nanocomposites. These recent development are particularly well described in the review of V. Buscaglia and M.T. Buscaglia [11]. As an example, the combination of size effects and local composition gradients has led to nanoceramics exhibiting reasonable tunability, moderate dielectric losses and flat temperature-independent permittivity [19].

A key point in the processing of core-shell designed ceramics is the sintering step mandatory to obtain dense ceramics. Expecting new properties compared to homogeneous systems or aiming to preserve the functionality of each component, the accurate control of interfaces, interdiffusion and defect chemistry during the sintering is a critical issue. Fast sintering techniques such as Spark Plasma Sintering have provided unique opportunities to yield highly densified ceramics with tailored microstructures [20, 21]. The simultaneous action of uniaxial pressure and pulsed electrical current ensures efficient heating leading to fast sintering kinetics [22]. It is worth noting that SPS ensures reproducibility of both microstructure and properties of ceramics of about 10-20mm diameter and ceramics can be processed

with thickness as low as 50-100µm, values in the range of those obtained by tape casting, a scalable process widely used in MLCC industry. The flexibility of SPS in terms of adjustable experimental parameters and their influence on properties will be illustrated in sections 3.1 and 3.2. The ceramics presented in these sections were performed using the Spark Plasma Sintering device (Dr Sinter SPS-2080 - Syntex Inc.) located at the Plateforme Nationale de Frittage Flash du CNRS, Université Toulouse III Paul Sabatier, France. The experimental conditions related to synthesis or sintering are detailed elsewhere in the corresponding references.

3.1 Silica and magnesium oxide coated ferroelectric particles

3.1.1 Silica based core-shell nanocomposites

The coating of oxide or metallic particles with a continuous silica shell has been applied to various inorganic materials to design functional materials at the nanoscale with controlled magnetic, optical, electronic or catalytic properties [23]. Using the seed growth process, we have successfully coated $BaTiO_3$ and $Ba_{1-x}Sr_xTiO_3$ (BST) particles with a continuous silica shell of thickness accurately controlled from 1 to 100nm (coated particles are noted BT@SiO_2, BST@SiO_2) [24] (Figure 1a). The critical step is the colloidal stabilization of the seeds before encapsulation or surface functionalisation. The first step is to improve the colloidal stability of the ferroelectric nanoparticles by nitric acid leaching in order to activate the surface sites. Then the hydrolysis/condensation of tetraethoxysilane (TEOS) is catalyzed by ammonia in alcoholic media. The core-shell approach in this context aims to create an artificial dielectric grain boundary. The silica layer coats individually each ferroelectric grain and plays the role of a dielectric barrier at the grain scale. In order to preserve the silica layer within the final dense ceramics, SPS was first performed at relatively low temperature (1050°C) and under argon [25]. These two conditions are mandatory to avoid both interdiffusion between the ferroelectric and dielectric phases and the reduction of Ti^{4+} into Ti^{3+} associated with the creation of oxygen vacancies. Indeed, BT ceramics obtained by SPS are usually performed under low oxygen partial pressure with sintering temperatures and applied pressures in between 800-1200 °C and 40-100 MPa, respectively. A post-sintering annealing under air in the temperature range 700 - 1000 °C is thus mandatory to minimize oxygen vacancies associated with the reduction of titanium Ti^{4+} into Ti^{3+} and to recover insulating properties (Ti^{3+} into Ti^{4+}). The defect chemistry at the grain boundaries is then hardly fully mastered, in particular in nanostructured ceramics [10, 26]. The combination of low temperature and inert atmosphere enabled to obtain BT@SiO_2 ceramics exhibiting high stability of permittivity over a wide temperature range and low dielectric losses at low frequency (0.5% at 10 kHz). However, the interdiffusion between the ferroelectric core and the dielectric shell cannot be completely avoided [25]. The broadband dielectric spectroscopy in the high-frequency range up to the infrared (IR) is a very sensitive tool to probe interdiffusion phenomena that causes an additional dielectric dispersion below the polar phonon range. The effective complex dielectric function in the IR-THz range was studied for nanoporous composites [27] and for $BaTiO_3$@$SrTiO_3$ and $BaTiO_3$@$BaZrO_3$ dense core-shell nanocomposites [28]. The

effective polar phonon response was compared with the prediction of appropriate effective medium approximation coated-spheres model. The observed enhanced THz and microwave absorption was qualitatively ascribed to an interdiffusion of $BaTiO_3$ cores into the shells [28]. Broad band dielectric spectroscopy was also used to probe the degree of interdiffusion of several $BaTiO_3$@SiO_2 nanostructured ceramics differing in the sintering temperature and thus in the level of densification [29]. An additional THz-Mw dispersion whose strength increased with the density of the ceramic (i.e. sintering temperature), was ascribed to gradient layers between core and shells. Bound charges connected with such interfacial gradient layer are supposed to be at the origin of the additional dispersion [29]. In a higher extent, such interfacial polarization is also well known as Maxwell-Wagner effect in inhomogeneous ceramics with grains boundaries more resistive than the grains. Grain boundary surface barrier layer capacitor effect is at the origin of giant permittivity in reduced $BaTiO_3$ [30], $CaCu_3Ti_4O_{12}$ [31] or in Nb+In co-doped TiO_2 with in this case the formation of localized electron-pinned defect dipoles [32, 33]. The broadband dielectric spectroscopy is also very useful to analyze the dielectric relaxation processes in the GHz and THz ranges linked to the defects associated with the giant permittivity behavior [34, 35]. Theoretical approaches have been also proposed to reproduce the giant permittivity behavior and to evaluate the potentiality of electrical energy storage and electrocaloric effect in the framework of a core-shell model of nanoceramics [36-38].

Using SPS in low partial oxygen pressure (reducing conditions) to sinter silica coated BT, tuned chemical reduction resulting in very large dielectric permittivity ($>10^5$) was achieved [39]. Even after a reoxydation step under air, the as obtained core-shell nanostructured ceramics exhibit a gradually deepening blue which, in a first attempt, can be ascribed to the existence of Ti^{3+} associated with oxygen vacancies. During the SPS ultra-fast cooling, the re-frozen silica shell acts as re-oxidation barrier which prevents from free charges mobility. As a result, stable Ti^{3+} ions are maintained in the ceramics and space charges are trapped at the interfaces. The most striking effect is the coexistence of giant permittivity and low dielectric losses (<5%) thanks to the silica phase. At the grain boundaries, the silica plays a dual role of dielectric and re-oxydation barrier [40]. However it was essential to reach a detailed knowledge of the nature and concentration of charged defects for both better understanding of the properties and material design by tailoring properties. Deep insights into the defect structure of oxides are facilitated by another very sensitive technique, the Electron Paramagnetic Resonance (EPR). Due to its high sensitivity EPR offers unique opportunity to study all kind of materials from bulk ceramics and composites, single crystals to thin films and nanosized powders. Operating in a wide temperature range (from cryogenic to high temperatures 2-700 K), EPR allows not only to identify charged defects and estimate their concentration, but also to study the lattice dynamics, the phase transitions: structural and magnetic, the relaxation and ions mobility processes. Valence changes of defects / defect complexes as a function of electronic charge trapping also can be monitored by EPR [12, 41, 42]. These features of EPR are of particular interest for understanding the defect chemistry crucial in functional materials. Temperature dependent electron paramagnetic resonance was undertaken

to confirm that the space charge relaxation observed in BT@SiO_2 ceramics sintered by SPS under vacuum is due to Ti^{3+} - V(O) charged defects [40]. The thermal activation of the Ti^{3+} EPR line was shown to follow the same Arrhenius law as the dielectric one with a common activation energy of 100 meV thus a direct link between the macroscopic dielectric relaxation and the microscopic dynamics of charged defects (Ti^{3+} - V(O)) was clearly evidenced [40] (Figure 1b).

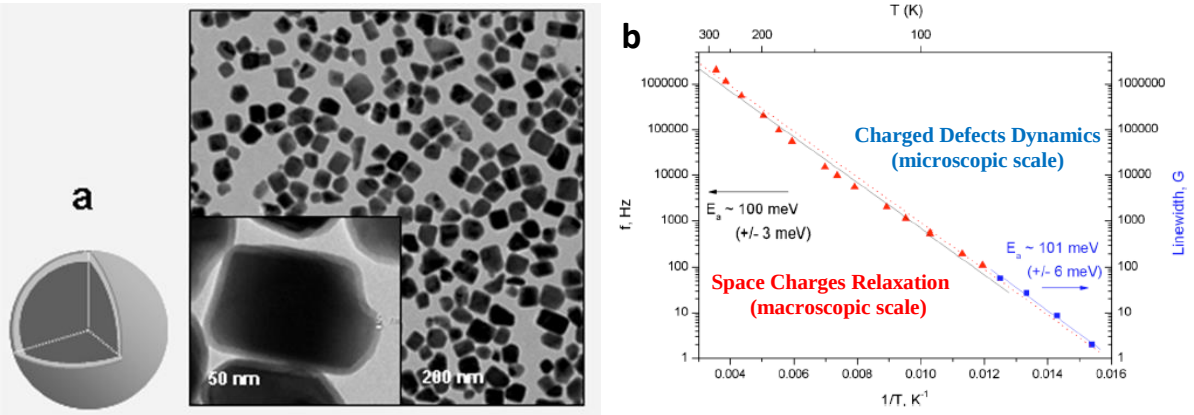

Figure 1. a) $BaTiO_3$ core embedded within a dielectric shell (silica), b) Link between macroscopic dielectric relaxation and microscopic dynamics of charged defects from electron paramagnetic resonance

Beyond amorphous silica coating, it was interesting to investigate a crystallized dielectric shell that could display in particular different sintering behavior. This was achieved considering a magnesium oxide shell as described in the following section.

3.1.2 Magnesium oxide based core-shell nanocomposites

Magnesium oxide was also widely used in ferroelectric/dielectric composites designed at the micro- and the nanoscale to decrease the dielectric losses while keeping moderate permittivity in the range 500-1000 [7, 8, 42]. Aiming once again a control of the dielectric phase at the grain scale, we successfully adapted an original method based on thermolysis process for an efficient coating on ferroelectric particles surface by a crystallized MgO shell [43]. The reaction occurs in solution at 290°C by thermal decomposition of the magnesium precursor, $Mg(acac)_2$, during heating at 290°C. Randomly oriented and crystallized MgO nanosized particles aggregate around BT particles (Fig. 2a). The initial core-shell architecture is transformed into a uniform distribution of sub-micrometric sized BT and MgO during sintering by SPS at 1100°C (pressure applied 2.5kN). The thermomechanical properties of MgO nanoparticles (soft plastic behavior) and their weak cohesion all around the ferroelectric cores allow a particle rearrangement in the early stages of SPS sintering as soon as the pressure is applied [44]. As a result, a homogeneous composite nanostructure is formed in-situ during sintering (Fig. 2b). The initial core-shell structure is lost after thermal treatment but the MgO still acts as a diffusion barrier which prevents the ferroelectric core from grain growth. The dielectric properties reflect the composite effect,

with especially low (≈0.5 %) and stable dielectric losses for a wide frequency range. A significant stabilization of the permittivity as a function of temperature is obtained in BT/MgO ceramics compared to BT ceramics sintered by SPS in similar conditions. This clearly reflects the impact of the stress generated in the BT particles during densification through the extended interfaces in between the two components (Fig. 2c) [43].

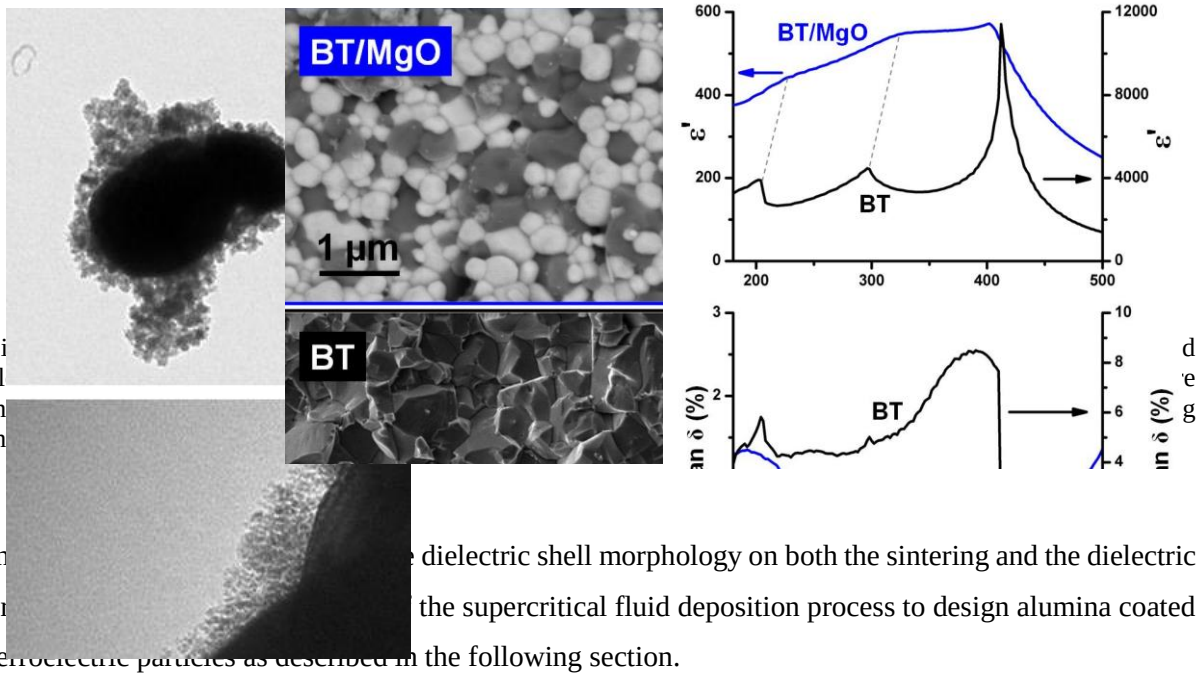

Fi d
el e
in g
in

In dielectric shell morphology on both the sintering and the dielectric pr the supercritical fluid deposition process to design alumina coated ferroelectric particles as described in the following section.

3.2 Surface functionalization of ferroelectric particles by supercritical fluid chemical deposition (SFCD) process

The unique properties of supercritical fluids are investigated for more than 25 years to design advanced functional materials [45]. A supercritical fluid is a solvent which is processed in specific conditions of pressure and temperature above its critical pressure (p_c) and temperature (Tc). It is important to underline that each fluid has a specific critical point. The most used fluids are CO_2 (p_c=73.8 bar and Tc=31 °C), H_2O (p_c=221 bar and Tc=374 °C), EtOH (p_c=6.27 bar and Tc=241 °C) or some mixtures of them as CO_2/EtOH. For mixtures, the critical point is evolving as a function of the composition. For instance, the evolution of the critical point of the mixture CO_2/EtOH can be found elsewhere [46]. The principle of the preparation of nanostructured materials using supercritical fluids consists in performing a chemical reaction in this solvent processed under specific conditions of pressure and temperature, the chemical reaction inducing the homogeneous nucleation & growth of the nanostructures. Numerous materials have already been synthesized in supercritical fluids [47] among the families of oxides, metals, nitrides, etc. Changing the solvents allows playing with chemistry and so with the nature of materials, for instance, from the formation of oxides in supercritical water to the formation of nitrides in supercritical ammonia. A first part of the research concerns the synthesis of nanopowders in continuous and scalable supercritical reactors for applications in electronics [48], in optics [49], in catalysis [50], in

environment [51], in geoscience [52], etc. A second part of the research is dedicated to material surface engineering by the controlled deposition of a material on a substrate surface know as Supercritical Fluid Chemical Deposition (SFCD) [53, 54]. This deposition method allows decorating the surface of a particle from supported nanoparticles to layered architecture (Figure 3a).

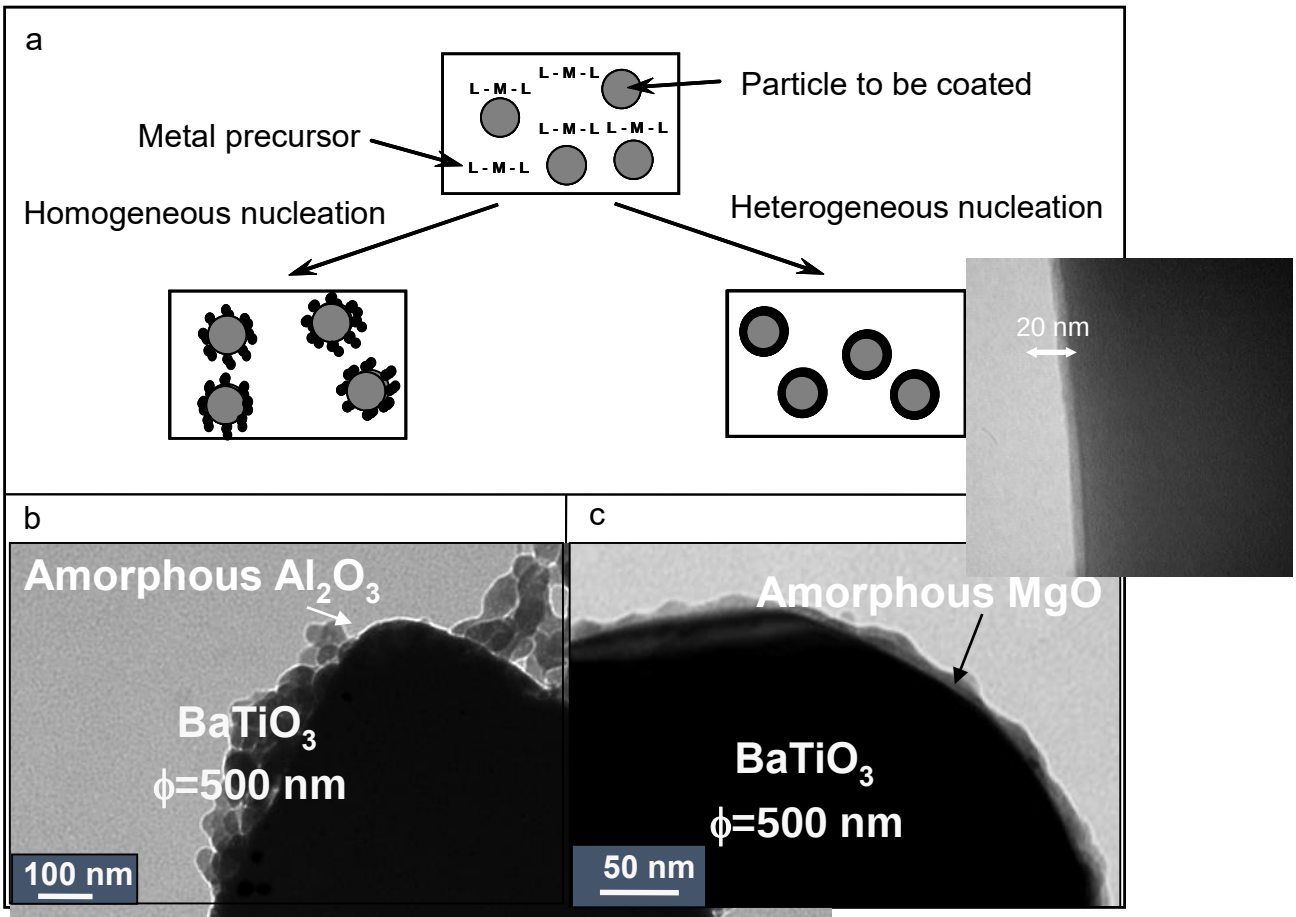

Figu… …a $BaTiO_3$ particle and c) shell of

In a… …pressure / high temperature reac… …nd CO_2 is added. The reactor is p… …transformation of the metal precursor and the deposition of nanostructures or a shell.

This surface modification method has been applied to the functionalization of $BaTiO_3$-based particles. $Ba_{1-x}Sr_xTiO_3$ (x=0 and x=0.4) particles were coated with alumina using aluminium acetylacetonate as metal precursor at 200 bar and 200 °C. The addition of 1%wt of titanium isopropoxide as catalyst conducts to a homogeneous nucleation of amorphous alumina nanoparticles. These nanoparticles are minimizing their surface energy by deposition at the surface of the ferroelectric particles, the result being the formation of a powder consisting of supported alumina nanoparticles on $Ba_{1-x}Sr_xTiO_3$ particles as shown on Figure 3b. In the absence of Ti-based catalyst in the reaction medium, there is a heterogeneous

nucleation and growth of a shell of amorphous alumina at the surface of the $BaTiO_3$-based particles (Figure 3a) [55]. At the end of the coating experiment, pure supercritical CO_2 passed through the reaction vessel to remove ethanol and organic residues from the aluminium precursor. A dried powder can be then recovered without any additional filtering and post-treatment and can be used as it for further processing to prepare ceramics. Only changing the nature of the metal precursor allows to change the nature of the coating. Replacing aluminium acetylacetonate with a magnesium precursor gives access to the formation of an amorphous magnesium oxide shell (Figure 3c).

SFCD functionalized nanopowders $BaTiO_3@Al_2O_3$ (noted $BT@Al_2O_3$), $Ba_{0.6}Sr_{0.4}TiO_3@Al_2O_3$ (noted $BST@Al_2O_3$) and $Ba_{0.6}Sr_{0.4}TiO_3@Al_2O_3$ NPs formed in presence of the catalyst (noted $BST@Al_2O_3$-C) were sintered by SPS. The objectives were (i) to preserve the core shell architecture within the final SPS ceramics, (ii) to determine the influence of the composition of the ferroelectric core (BST or BT) and the impact of the morphology of the coating (continuous alumina shell or supported alumina nanoparticles) on the structure and microstructure of the composite ceramics.

The optimized sintering conditions are reported in Table 1. They were selected considering (i) the minimization of grain growth and thus the preservation of the core shell design, (ii) the limitation of the reduction of Ti^{4+} into Ti^{3+} associated with the creation of oxygen vacancies under vacuum at high temperature [26, 39, 40] and (iii) the control of interdiffusion at the interface between the ferroelectric core and Al_2O_3 to prevent the formation of barium aluminate (*BAO* = $BaAl_2O_4$) interphase.

Temperature Set Point (°C)	Pulse Sequence (On-Off)	Dwell time (min)	Heating rate (°C/min)	Applied Pressure (MPa)	Atmosphere
1100	12-2	3 to 5	100	100	Vacuum

Table 1. Optimized Spark Plasma Sintering conditions

Further, it is well-know from Finite Element simulations of the SPS process, particularly when insulating materials are sintered, that the current distribution in the tool may induce temperature gradients, overheating of the punches and of the graphite sheet lining the inner wall of the mold [56, 57]. To minimize these phenomena and homogenize the temperature within the sample, two alumina buffer layers have been added on each side of it. It turns out that the two alumina buffers are also efficient to minimize titanium reduction as confirmed by the color of ceramics i.e. ceramics of white color were systemically obtained.

The structural investigation by XRD of the different SPS ceramics indicates that both the composition (*BST compared to BT*) and the morphology of the alumina shell play a role in the BAO interphase formation. Interdiffusion is minimized in the case of $BST@Al_2O_3$ ceramics compared to BT ones. In

addition, when the shell is made of supported alumina nanoparticles, a significant decrease in the amount of BAO is observed whatever the composition of the ferroelectric core. An illustration is given on Figure 4 for BST composites.

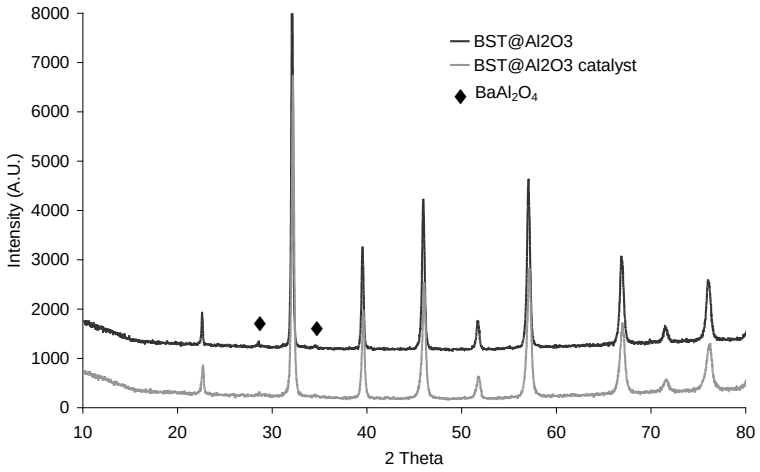

Figure 4 XRD of SPS sintered BST@Al_2O_3 and BST@Al_2O_3-C (with catalyst)

Whatever the composition of the core and the morphology of the shell, SPS moderate conditions allowed to obtain high relative density ceramics (> 90%). It has to be noted that the alumina coating hinders the densification since for ceramics made of uncoated particles (BT and BST), relative density higher than 95% are obtained for similar sintering conditions [26].

The microstructure evaluated by SEM revealed the absence of grain growth for the BT composite ceramic compared to the starting powder (particle size 500nm), which can be ascribed to the presence of the alumina shell and to the moderate sintering conditions used (Figure 5a). In the case of the BST composite ceramics, even though BST is more refractory than BT [58], an increase of the grain size is observed after sintering (from initial powder 200nm to final grain size about 500nm) (Figure 5b). The grain growth could be explained by a higher reactivity of the BST due to smaller initial particle size compared to BT.

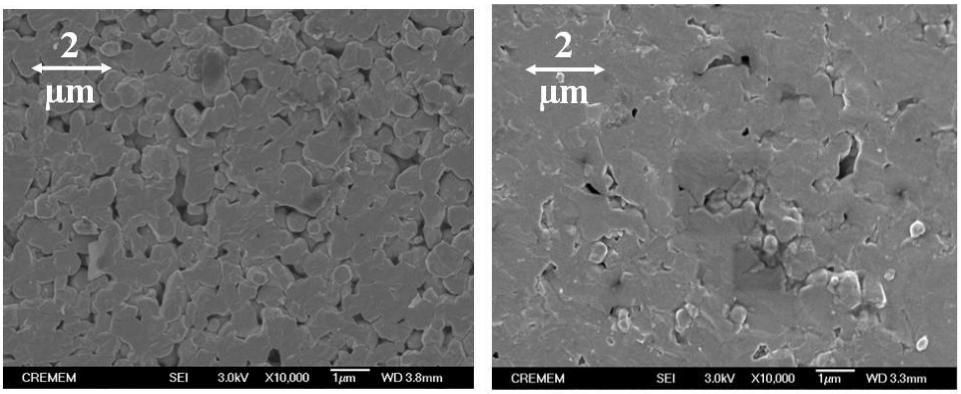

Figure. 5. SEM images of SPS ceramics: a) BT@Al_2O_3 and b) BST@Al_2O_3

Whatever the SPS core-shell ceramics, dielectric characterizations show that the contribution of alumina strongly decreases the dielectric permittivity compared to BT and BST ceramics. For BT@Al_2O_3 ceramic, the BAO secondary phase may contribute to lower even more the permittivity but does not affect the ferroelectric properties as the Curie temperature remains close to 402K. As expected, thanks to the dielectric shell, the dielectric losses remain below 1% at room temperature. Similarly, for the BST composite ceramics, the Curie temperature occurs close to 260K as expected for composition $Ba_{0.6}Sr_{0.4}TiO_3$. Room temperature permittivity of the BST composites also depends on the morphology of the alumina shell. A permittivity value close to 3100 is observed when BST grains are coated with a continuous alumina shell (Figure 6). For BST with supported alumina particles, permittivity value is about 2200. This trend was not expected considering the absence of BAO phase in BST@Al_2O_3-C ceramic. This discrepancy has to be related to the level of porosity which is higher in the latter sample compared to the others and that could lead to lower value of permittivity. Similarly to BT based composites, the dielectric losses of BST based composites are also lower than 1% at room temperature. Both the flattening of the dielectric permittivity and the reduction of losses well below 1% over an extended temperature range make these core-shell composites appealing for applications.

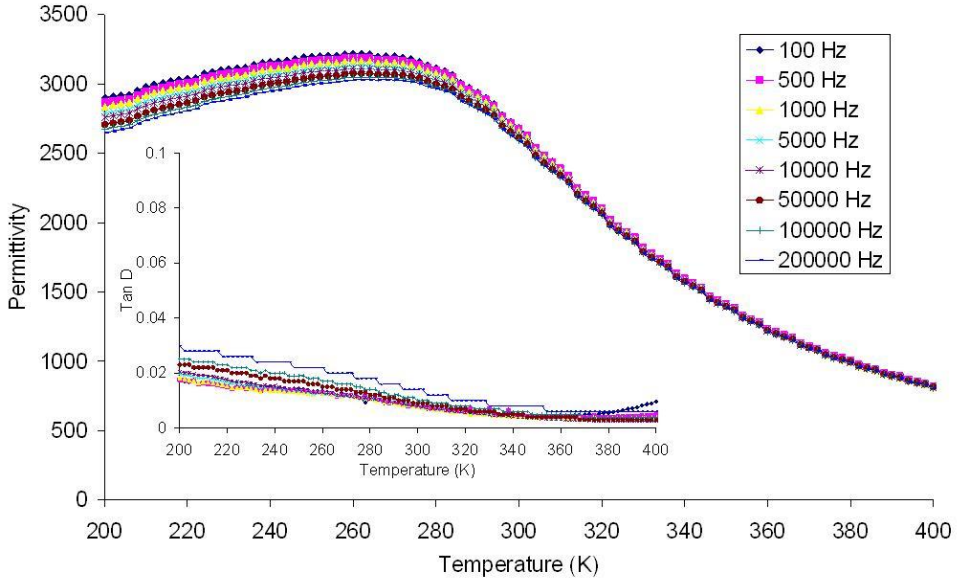

Figure 6. Temperature dependence of the permittivity and dielectric losses (Tanδ) in the frequency range 100Hz-200 kHz for BST@Al_2O_3 ceramic sintered by SPS

The flexibility of the core-shell approach was illustrated in the two previous sections through the design of shells with different nature, morphology and crystallinity and their impact on both microstructure and dielectric properties. The advanced synthesis methods presented allowed to create an artificial dielectric grain boundary whose nature and thickness can be finely controlled. Controlling such high density of interfaces remains challenging during the sintering. SPS was shown as a remarkable versatile technique

that enables to yield original 3D nano/microstructures. Regarding the properties, an obvious advantage of the core@shell approach lies in the existence of extended interfaces between the components in all directions. This is particularly interesting and attractive to promote magneto-dielectric coupling. Alternatively to the architectures mentioned above, the core–shell approach can therefore also be exploited to target multifunctional composites. This will be illustrated in the next section through i) silica based 3D composites and ii) one dimensional (1D) nanostructures that coaxially combine electric and magnetic materials.

4. Complex core-shell based architectures toward multifunctionality

Magnetoelectric (ME) composites made by combining ferroelectric and magnetic phases are a novel class of next generation of multifunctional materials that have drawn significant interest in recent years [59-63] In particular, the indirect strain mediated coupling interaction between piezoelectric and magnetostrictive phases could produce a large ME response, several orders of magnitude higher than that corresponding to single phase ME materials so far available at room temperature. This ME effect in composite materials is known as a product tensor property which results from the cross interaction between piezoelectric and magnetostrictive ordering of the two phases [59, 60, 63]. ME composite architectures have been prepared in several geometries like particles embedded in a matrix [64, 65], co-sintered bilayered structures [66, 67], as well as low-dimensionality heterostructures such as laminated and epitaxial self-assembled vertical thin-films or more recently, coaxial nanofibers [68-71].

We present in this section two illustrations based on the core-shell approach to reach multifunctionality targeting magnetoelectric nanostructured compounds: ferroelectric/magnetic nanorasberries and nanocables.

4.1 Ferroelectric/Magnetic Raspberries

Starting from silica coating that allows a further functionalization of the ferroelectric nanoparticles, innovative 3D ferroelectric/magnetic nanocomposites with extended interfaces between the two components were designed to promote magneto-dielectric coupling. We have demonstrated the possibility to obtain ferroelectric/magnetic raspberry building blocks from $Ba_{0.6}Sr_{0.4}TiO_3$ (BST) and $BaTiO_3$ (BT) ferroelectric grains coated by silica and covered with 7 nm diameter γ-Fe_2O_3 nanoparticles also coated by silica (Figure 7a-b). The method used to prepare ferroelectric/magnetic raspberry building blocks involves: the silica coating of ferroelectric cores previously described [24]; the surface modification of the silica core-shell ferroelectric particles by an aminosilane coupling agent in order to provide positively charged surface. Due to the negative charge of magnetic@SiO_2 nanoparticles, nanoraspberries morphologies are formed by the simple mixing of the two colloidal systems by electrostatic interactions [72]. The main challenge is to find the best pH conditions for better electrostatic interactions between the aminated BST (or BT)@ SiO_2 particles and the γ-Fe_2O_3@SiO_2 nanoparticles while preserving the stability of both colloidal dispersions. Nanostructured ceramics with the

coexistence between ferroelectricity, piezoelectricity and superparamagnetism were clearly evidenced at room temperature [72]. However no magneto-electric coupling was found probably because of the limited strain mediated interactions between both components resulting from the presence of silica as an intermediate phase. This is why we looked for nanostructures in which the ferroelectric and ferromagnetic phases are in direct interaction, namely nanocables that are described below.

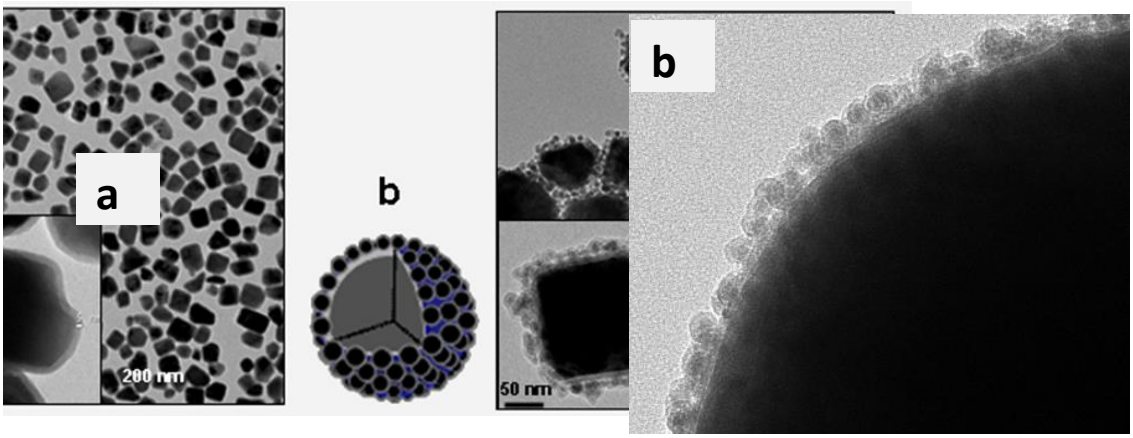

Figure 7. a) View of several raspberries nanoparticles formed of $BaTiO_3$ core embedded within a silica shell and coated with a supplementary magnetic nanoparticles embedded within an ultrathin silica shell, b) Zoom on the surface.

4.2 (1D) nanostructures that coaxially combine electric and magnetic materials.

Another approach to design core-shell multiferroic nanostructures is to use template-assisted synthesis methods. Due to their reliability, flexibility, and reproducibility, template-assisted synthesis attracts a significant interest to build well-ordered three-dimensional arrays of nanowires (NWs) with high aspect ratio and high surface areas [73-75]. In a previous work, we have reported the two-steps synthesis of $BaTiO_3$-Ni (BTO-Ni) nanocable (NC) arrays within porous anodic aluminium oxide (AAO) templates [76]. The limitations inherent to a thermal treatment performed at high temperature were pointed out. It was shown that the thermal annealing required for BTO crystallization can (i) affect the ferroelectric BTO shell microstructure through defects-driven surface rearrangement and diffusion inside the AAO pores, and (ii) induce the template curvature, hence hindering the subsequent Ni electrodeposition into the BTO-coated AAO pores. The strength of the dipolar interaction arising from the packing density of the magnetic nanowires was correlated to the $BaTiO_3$ wall thickness through magnetometry and ferromagnetic resonance measurements [76]. Magnetic properties of such core-shell nanowires can be tuned by an appropriate choice of membrane, packing fraction, geometric parameters (*i.e.*, core radius and shell thickness) and composition.

Meanwhile, in order to favour electromagnetic coupling, core-shell composites made of $PbZr_{0.52}Ti_{0.48}O_3$-$CoFe_2O_4$ (PZT-CFO) are very appealing, as PZT with composition near the morphotropic phase boundary (MPB) exhibits excellent FE and piezoelectric properties, whereas CFO displays large magnetocrystalline anisotropy, high coercivity, and moderate saturation magnetization [77]. Most of the

studies devoted to coaxial PZT-CFO were based on electrospinning of nanofibers [71] and sol-gel deposition of nanowires into AAO pores [78,79]. Past efforts on ME characterization of core-shell nanofibers involving piezoresponse force microscopy (PFM) performed on a single PZT-CFO and BTO-CFO nanofibers showed large ME coefficients of 29.5 and 35 V cm^{-1} Oe^{-1}, respectively [71, 80]. Recently, direct ME coefficient of 450 µV cm^{-1} Oe^{-1} was measured using a small *ac* magnetic field values with variation in the *dc* magnetic field for disks made of BTO shell-NFO core nanofibers prepared using magnetic field assisted assembly of fibers into planar film [81]. The relatively low ME coefficient value was ascribed to several contributions: air gaps, voids, porosity, defects in the assembly, and dipole-dipole interactions between magnetic cores. Therefore, to obtain large ME voltage coefficient in core-shell nanofibers/nanowires arrays, large interfacial surface area between two constituents has to be enhanced and their morphology (i.e. voids, porosity, ratio of core-to-shell radius, shells wall thickness), structural properties (i.e. defects, diffusion), and dipolar interactions between magnetic cores in core-shell nanofibers assembly (i.e. magnetic cores packing density) have also to be controlled.

Our approach aimed the elaboration of vertically oriented arrays of PZT-CFO core-shell nanocables (NCs) using a three-step process: (i) sol-gel dip-impregnation of porous anodic aluminium oxide (AAO) templates (Synkera, Co) and crystallization of the PZT shell on the pore walls, thus forming PZT nanotubes (NTs), (ii) $CoFe_2$ metallic alloy pulsed electrodeposition within the PZT-coated AAO templates, and (iii) *in situ* oxidation of the $CoFe_2$ to obtain the desired CFO spinel cores. The different steps of the fabrication process are schematically illustrated in Figure 8.

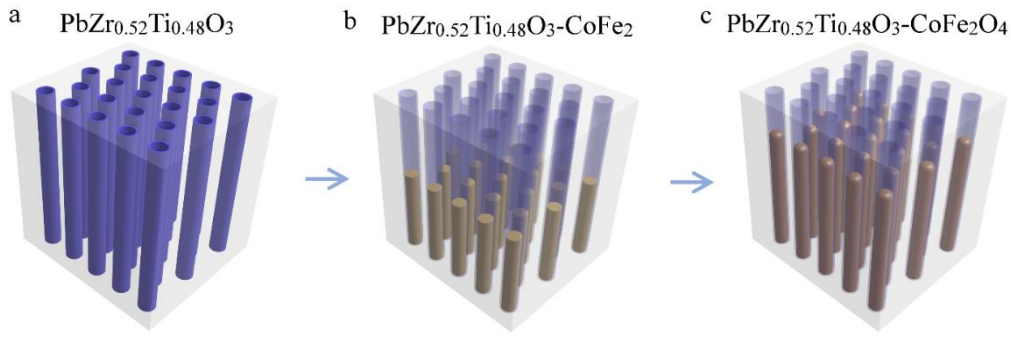

Figure 8. Schematics for the synthesis of the CFO-PZT NC arrays: (a) wet chemical deposition and crystallization of the PZT shells on the pore walls of the AAO template, (b) pulsed electrochemical deposition of the $CoFe_2$ cores within the PZT-coated AAO pores, and (c) $CoFe_2$ conversion into CFO phase by *in situ* thermal oxidation.

Taking into account the above-mentioned temperature-related limitations on the control of interfaces, we took advantage of the flexibility of the impregnation–electrodeposition approach to lower the processing temperatures and thus improve nanocables's microstructure while ensuring chemical integrity of the two-phase materials. In particular, the benefit of the direct *in situ* oxidation of the metal $CoFe_2$ nanowires into the metal oxide CFO nanowires during the crystallization of PZT nanotubes was demonstrated and the role of PZT nanotubes as a diffusion barrier was highlighted.

Magnetic and piezoresponse force microscopy (PFM) characterizations were conducted to study magnetic and ferroelectric properties at the microscale of the as-prepared core-shell PZT-$CoFe_2$ and PZT-CFO nanocable arrays. In order to avoid critical size effects [82-84] and to preserve the ferroelectricity in PZT nanotubes, sidewalls were thickened by repeating the sol-gel dip-impregnations

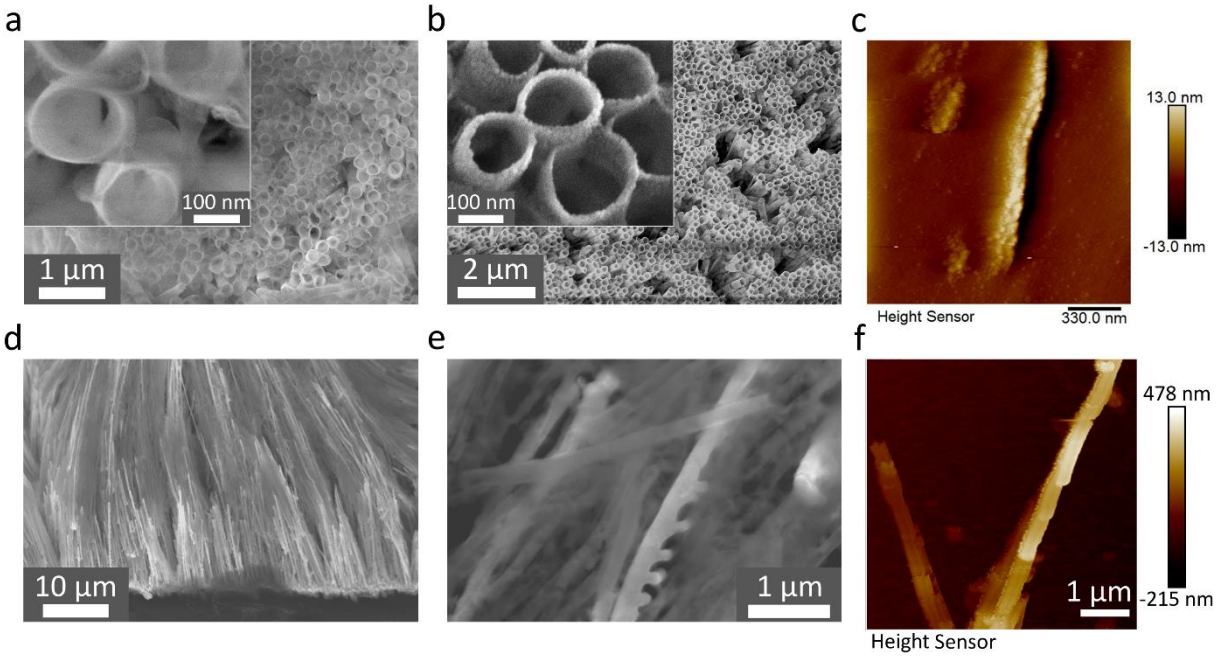

Figure 9**. (a,b)** HRSEM images of free-standing PZT^{500} nanotubular structures (D_{pore} ~150 nm, P_{AAO} ~35 %) prepared using **(a)** one and **(b)** three consequent sol-gel dip-impregnations into AAO templates. Tapping mode AFM topography image **(c)** of the three-layer PZT^{500} NT collected on the Pt/Si substrate. **(d)** Tilted top view SEM image of the PZT_{500}-$CoFe_2$ nanocables after the partial dissolution of AAO template. **(e)** Top view SEM images of the PZT^{500}-$CoFe_2$ NC arrays after the full AAO dissolution. **(f)** Tapping mode AFM topography image of the PZT^{500}-$CoFe_2$ nanocables.

three times. Figures 9a and b show the top view SEM images of the PZT NT arrays calcinated at low temperature 500°C (noted PZT^{500}), in the case of single PZT tubular layer (Figure 9a), and three PZT tubular layers (Figure 9b) into AAO membranes (D_{pore} ~150 nm, P_{AAO} ~35 %) with pores length around 50 µm. From SEM observations, the average wall thickness of the PZT nanotubes was estimated in the range of 5-10nm for single-layer PZT and in the range of 10-20 nm for three-layer PZT. Figure 9c shows 2×2 µm^2 tapping mode AFM topography image for a PZT nanotube deposited on a Pt/Ti/Si substrate. The AFM images confirm the granular morphology of the PZT nanotubes.

Metallic $CoFe_2$ nanowire arrays were then grown inside PZT^{500}-coated AAO membranes using a pulsed electrodeposition process. Figures 9d and e show the tilted top view SEM image of the as obtained PZT^{500}-$CoFe_2$ nanocables after the partial and complete dissolution of the AAO membrane, respectively. An average height of the PZT^{500}-$CoFe_2$ nanocables was estimated as expected close to ~10 µm. The filling of the PZT^{500} was homogeneous and the $CoFe_2$ growth was stopped after 3000 seconds when the deposited nanowires height, h_{NW}, was about 10 µm. EDX analysis (not shown) confirms the composition of $PbZr_{1-x}Ti_xO_3$: x = 0.47 for the PZT^{500} nanotubes, which is close to the PZT morphotropic phase boundary region with x=0.48. Note that the atomic ratio of Pb has reduced by about 15%, which can be

a result of partial diffusion at PZT/AAO interfaces. The Fe/Co ratio close to 2 was confirmed. Figure 9f shows tapping mode AFM topography image, respectively, taken on a PZT^{500}-$CoFe_2$ nanocables with outer diameter ~150 nm. The topographic AFM images indicate a smooth surface with low roughness of the PZT^{500}-$CoFe_2$ nanocables.

The ordered arrays of AAO-embedded PZT^{500}-$CoFe_2$ nanocables were magnetically characterized to determine the impact of the nanocable architecture on the magnetic properties. For the arrays of metallic $CoFe_2$ nanowires, the magnetocrystalline anisotropy can be neglected and the effective field, H_{eff}, in the saturated state is only determined by magnetostatic contributions, i.e. shape anisotropy and dipolar interaction. It can be thus expressed as $H_{\text{eff}} = 2\pi M_s - 6\pi M_s P_{\text{NW}}$ [85] where P_{NW} is the nanowires packing factor and M_s ~1900 emu cm^{-3} is the saturation magnetization for $CoFe_2$ [77]. Figure 10 shows the normalized magnetic hysteresis loops measured at room temperature using alternating gradient magnetometer (AGM) with the field applied along the in-plane (perpendicular to nanowire axis) and out-of-plane (parallel to the revolution axis of nanowires) for $CoFe_2$ nanowire arrays as reference (Figure 10a), and two PZT^{500}-$CoFe_2$ core-shell nanocables arrays, corresponding to one dip and three dip PZT impregnation (Figures 10 b,c). Figure 6a reveals that the high packing density of $CoFe_2$ nanowires results in the easy direction of magnetization along in-plane direction ($P_{\text{CF35\%}} \sim 0.35 \pm 0.11$). The single layer PZT^{500}–$CoFe_2$ nanocables show almost isotropic magnetic behaviour due to the packing factor of $CoFe_2$ cores close to ~0.3 (Figure 10b). The three-layer PZT^{500}-$CoFe_2$ nanocable arrays are more easily

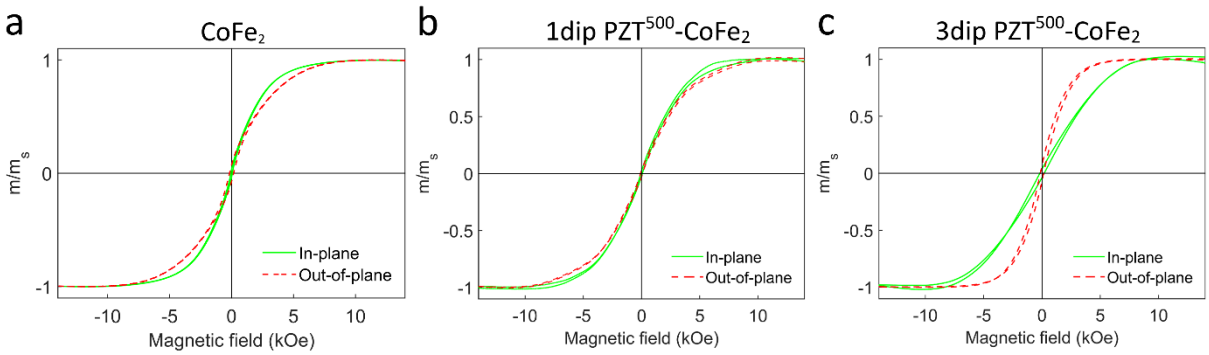

Figure 10. Room temperature hysteresis loops along in-plane (solid line) and out-of-plane (dashed line) directions for a vertically aligned $CoFe_2$ nanowire array **(a)** and the PZT^{500}-$CoFe_2$ multiferroic nanocable arrays consisted of single-layer **(b)** and three-layer PZT nanotubes **(c)**.

magnetized in out-of-plane direction which can be explained by the nanocable morphology and a packing factor P_{NW} =0.22, smaller than those of both purely metallic $CoFe_2$ nanowires and single layer PZT^{500}-$CoFe_2$ nanocables. Thereby, by tuning PZT shells sidewall thickness the easy magnetization axis and dipolar interaction between $CoFe_2$ cores in the PZT-$CoFe_2$ nanocable arrays can be controlled.

The oxidation of $CoFe_2$ to CFO inside pre-annealed three layers PZT^{500}, tubular structures was confirmed by *in situ* X-ray diffraction [86]. The metallic $CoFe_2$ and the oxide CFO coexist over a temperature range going from 300 °C to 500 °C.

For PZT^{500}-CFO^{600} core-shell nanocables ($CoFe_2$ oxidized at 600 °C), the magnetocrystalline anisotropy is dominant and an isotropic hysteresis behaviour regardless of the direction of applied magnetic field and large value of coercivity are observed.

One of the challenging step in the characterization of the core-shell nanocable is the macroscopic evidence of PZT nanotubes ferroelectricity, since it is not possible to apply electrodes as for thin-films. Some attempts have been made by polishing the membrane and depositing the top aluminium electrodes of ~1 µm thickness using thermal evaporation [78] but large leakage currents did not allow to observe a clear *P-E* hysteresis loop, unless the measurement frequency is increased to 100 kHz [87].

Local probe measurements using PFM were used in this work to confirm the polarization switching and local ferroelectric properties of three-layers PZT^{500} nanotubes and PZT^{500}-$CoFe_2$/CFO nanocables. PFM measurement of core-shell nanocable is schematically shown in Figures 11a. Figures 11b,c show PFM amplitude (b), and phase (c) images of PZT^{500}-$CoFe_2$ nanocables. The phase image (Figure 11c) do not clear show piezoelectric domains except a darker halo on the borders of the nanocable. However, this may be due to a topographic effect.

In addition, electromechanical amplitude and phase hysteresis loops were measured for PZT^{500} nanotube, PZT^{500}-$CoFe_2$ and PZT^{500}-CFO nanocables (Figures 11 d-f). First, PZT nanotubes and nanocables were identified by AFM imaging in tapping mode (see Figures 9 c,f), and then the phase and

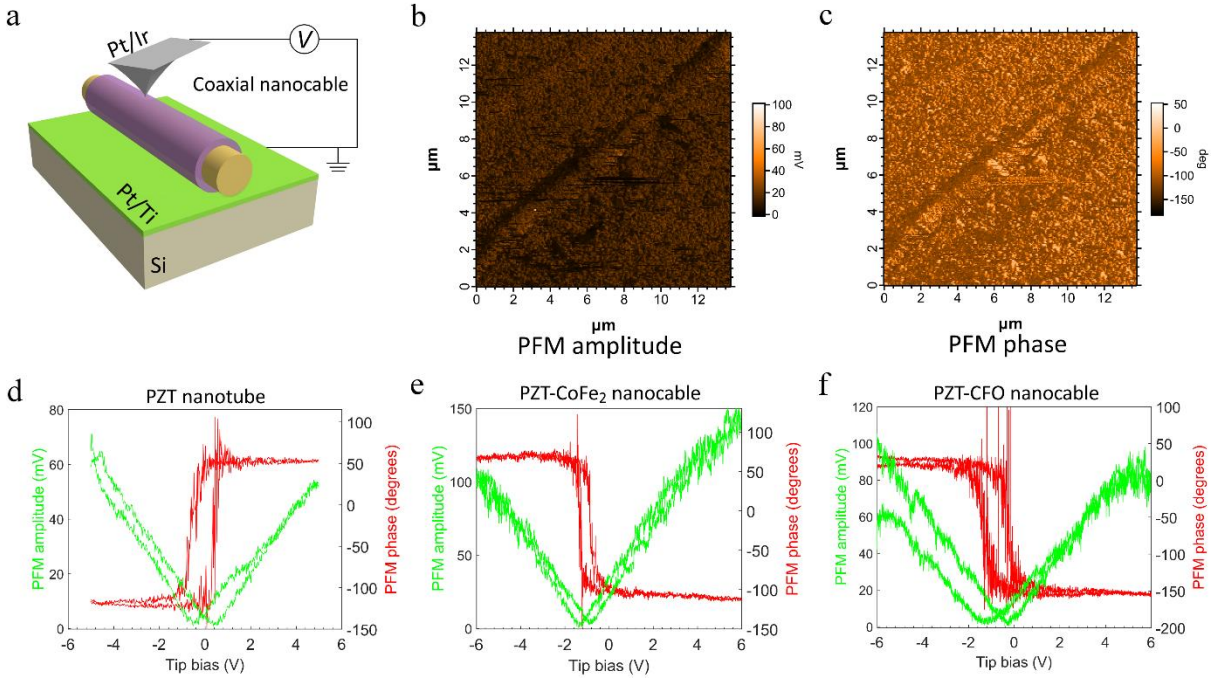

Figure 11. **(a)** Schematic of localized ferroelectric characterization of nanotubes and core-shell nanocables. PFM amplitude **(b)**, and phase **(c)** of the PZT^{500}-$CoFe_2$ nanocables. Domain switching shown by in-field phase (red line) and amplitude (green line) hysteresis loops for **(d)** the three-layer PZT^{500} nanotube, **(e)** the PZT^{500}-$CoFe_2$ nanocable, **(f)** the PZT^{500}-CFO^{600} nanocable prepared using three-layer PZT^{500} shells.

amplitude piezoresponse signals were measured in the central region of the nanotube or nanocable while ramping the *dc* bias voltage between -6 V and 6 V [88]. Figures 11 d-f show the phase (red line) and amplitude (green line) hysteresis loops measured in the central region of the PZT^{500} (d), PZT^{500}-$CoFe_2$ (e), and PZT^{500}-CFO^{600} (f). The PFM amplitude hysteresis show typical butterfly loops for all samples but in the case of PZT^{500}-$CoFe_2$/CFO nanocables (Figure 11 e,f, respectively), negative shifts of coercive fields in the phase and amplitude hysteresis were observed, which can be attributed to the presence of surface charges at the interface between $CoFe_2$/CFO cores and PZT^{500} shells. The phase variation in the PZT^{500} nanotube was around 170° after the *dc* bias voltage was increased from -5 to +5 V, and for the PZT^{500}-$CoFe_2$ and PZT^{500}-CFO^{600} nanocables with voltage changing from -6 to +6 V the phase change was around 180°. The domain switching voltages were (+0.4) – (-0.5) V, (-0.9) – (-1.3) V, and (-0.4) – (-1.3) V for the PZT^{500} nanotube, and PZT^{500}-$CoFe_2$ and PZT^{500}-CFO nanocables, respectively.

Despite we overcame the thermal constraints and demonstrated the benefit of a global lowering of the processing temperatures to preserve both architecture and structural integrity, some decisive parameters such as the uniformity of PZT wall thickness and the full oxidation of $CoFe_2$ cores need further optimization to obtain functional ME core-shell nanocables. Nevertheless, the control of interfaces at the nanoscale in such complex system opens a promising pathway towards low-cost processing of magnetoelectric nanocomposites.

5. Conclusion

The design of functional oxide materials with tailored properties remains challenging. This is particularly true in highly polarizable materials such as ferroelectrics which are highly sensitive to unavoidable defects, size effects and microstructure. Electrical breakdown strength, electrical conductivity, domain switching or electric-field induced strain are strongly dependent on charged point defects and microstructural features. Surface and interface-related phenomena are thus key issues in order to control the properties of nanostructured ferroelectrics based materials. Core-shell approaches leading to either chemical or structural gradients at the grain scale or modification / functionalization of particle surface have provided a significant contribution towards the control of properties through interface engineering. We have focused here on the core-shell composites approach in which the chemistry and defect chemistry can be modulated at the nanometer scale. We have shown that advanced chemical tools and specific synthesis path enable the building of individual (nano)-objects prior to their assembly and sintering to get functional materials with improved dielectric and magneto-electric properties. In particular, the flexibility of soft chemistry and Supercritical Fluid Chemical Deposition combined to Spark Plasma Sintering allowed for an accurate control of interfaces. We have underlined the crucial role of broad range spectroscopies to probe the defects at interfaces and to model the dielectric response of such architectured materials. These techniques are necessary to link microscopic and

macroscopic properties and to confirm that interfaces are not detrimental and even in some cases improve the materials performances.

If the promise of the core-shell composites has already been demonstrated in the field of ferroic materials, some clues for further improvements and future advances can already be identified. Deeper comprehensive studies of the grain boundaries structure at the atomic scale should be achieved thanks to high resolution electron microscopy and atom probe facilities. Chemical segregation, interdiffusion, defects spatial distribution, residual stress are decisive features that should be accurately mapped. A global lowering of the processing temperatures including the sintering would enable a better control of interfaces and improved dielectric and magneto-electric properties as already anticipated. Such development of energy effective and sustainable processes are under progress to widen the fields of application and to open the way for the integration of a large variety of functional ceramics and composites.

Acknowledgments

The IDS-FunMat European doctoral school is acknowledged for financial support. This work was partly supported by the Fédération Wallonie-Bruxelles (ARC 13/18-052, Supracryst) and by the Fonds de la Recherche Scientifique—FNRS under Grant no. T.0006.16.

Financial support from the French National Center for Scientific Research (CNRS), and the National Research Agency (ANR) (Projects NANO4F (ANR-05-JCJC-0169) and ARCHIFUN (ANR-12-BS08–009) are gratefully acknowledged.

References

[1] Y. Sakabe, N.Wada and Y. Hamaji, Grain size effects on dielectric properties and crystal structure of fine-grained BaTiO3 ceramics, *J. Korean Phys. Soc*. **32**, S260, **1998**.

[2] M.D. Glinchuk, I.V. Kondakova, V.V. Laguta, A.M. Slipenyuk, I.P. Bykov, A.V. Ragulya and V.P. Klimenko. Size Effects in Radiospectroscopy Spectra of Ferroelectric Nanopowders., *Acta Physica Polonica A*, **108**, 47, **2005**.

[3] J. F. Ihlefeld, D. T. Harris, R. Keech, J. L. Jones, J-P. Maria, S. Trolier-McKinstry, Scaling Effects in Perovskite Ferroelectrics: Fundamental Limits and Process-Structure-Property Relations., *J.Am.Ceram. Soc.*, **99**, 2537, **2016.**

[4] Nanoscale Ferroelectrics and Multiferroelectrics: key processing and characterization Issues, and nanoscale effects, Edited by M. Alguero, J. M. Gregg and Liliana Mitoseriu, John Wiley & Sons, Ltd, Chichester, UK **2016.**

[5] D. Hennings and G. Rosenstein, Temperature-Stable Dielectrics Based on Chemically Inhomogeneous $BaTiO_3$, *J.Am.Ceram. Soc.*, **67**, 249, **1984.**

[6] C. Elissalde, U-C. Chung, G. Philippot, J. Lesseur, R. Berthelot, D. Sallagoity, M. Albino, R. Epherre, G. Chevallier, S. Buffière, A. Weibel, D. Bernard, J. Majimel, C. Aymonier, S. Mornet,

C. Estournès and M. Maglione., Innovative architectures in ferroelectric multi-materials: Chemistry, interfaces and strain, *J. Adv. Diel.* **5**, 1530001, **2015**.

[7] S. Agrawal, R. Guo, D. Agrawal and A. S. Bhalla, Dielectric tunability of BST: MgO composites prepared by using nano particles, *Ferroelectr. Lett*. **31**, 149, **2004**.
[8] J. Lesseur, D. Bernard, U-C Chung, C. Estournès, M. Maglione and C. Elissalde, 3D mapping of anisotropic ferroelectric/dielectric composites, J. of Eur. Ceram. Soc., **35**, 337, **2015**.

[9] L. Padurariu, L. Curecheriu, C. Galassi & L. Mitoseriu., Tailoring non-linear dielectric properties by local field engineering in anisotropic porous ferroelectric structures, *Appl Phys Lett*, **100**, 252905, **2012**.

[10] M. Maglione, G. Philippot, D. Levasseur, S. Payan, C. Aymonier and C. Elissalde, Defect chemistry in ferroelectric perovskites: long standing issues and recent advances, *Dalton Trans.,* **44**, 13411, **2015.**

[11] V. Buscaglia and M.T Buscaglia, Core-Shell Heterostructures: From Particle Synthesis to Bulk Dielectric, Ferroelectric, and Multiferroic Composite Materials, Chapter 3 in Nanoscale Ferroelectrics And Multiferroics: Key Processing and Characterization Issues, and Nanoscale Effects, Volume I & II, (eds M. Algueró, J. M. Gregg and L. Mitoseriu), John Wiley & Sons, Ltd, Chichester, UK. **2016**.

[12] A. M. Slipenyuk, I. V. Kondakova, M. D. Glinchuk, and V. V. Laguta. Investigation of ferroelectric nanopowders by EPR method., *Phys. Stat. Sol.C* **, 4**, 1297, **2007**.

[13] V. Bovtun, S. Kamba, S. Veljko, D. Nuzhnyy, J. Kroupa, M. Savinov, P. Vaněk, J. Petzelt, J. Holc, M. Kosec, H. Amorín, and M. Alguero, Broadband dielectric spectroscopy of phonons and polar nanoclusters in $PbMg_{1/3}Nb_{2/3}O_3$–$PbTiO_3$ ceramics: Grain size effects, *Phys. Rev. B,* **79**, 104111, **2009.**

[14] J. Petzelt, D. Nuzhnyy, V. Bovtun, M. Savinov, M. Kempa, I. Rychetsky, Broadband dielectric and conductivity spectroscopy of inhomogeneous and composite conductors, *Phys. Status Solidi A*, **210**, 2259, **2013**.

[15] T. R. Armstrong and R. C. Buchanan, Influence of core-shell grains on the internal stress state and permittivity response of Zirconia-Modified barium Titanate, *J. Am. Ceram. Soc.,* **73**, 1268, **1990.**

[16] C. A. Randall, S. F. Wang, D. Laubscher, J. P. Dougherty, and W. Huebner, Structure property relationships in core-shell BaTiO3-LiF ceramics, *J. Mater Res,* **8,** 871, **1993.**

[17] I. Burn, "Temperature-Stable Barium Titanate Ceramics Containing Niobium Pentoxide, *Eleclrocomponent Sci. Techno.,* **2**, 241, **1976**.

[18] H. Kishi, Y. Okino, M. Honda, Y. Iguchi, M. Imaeda, Y. Takahashi, H. Ohsato and T. Okuda, The effect of MgO and rare-earth oxide on formation behavior of core-shell structure in $BaTiO_3$, *Jpn J Appl Phys*, **36**, 5954, **1997.**

[19] M. Airimioaei, M. T. Buscaglia, I. Tredici, U. Anselmi-Tamburini, C. E. Ciomaga, L. Curecheriu, A. Bencan, V. Buscaglia and L. Mitoseriu, $SrTiO_3$–$BaTiO_3$ nanocomposites with temperature independent permittivity and linear tunability fabricated using field-assisted sintering from chemically synthesized powders, *J. Mater. Chem. C,* **5**, 9028, **2017**.

[20] R. Chaim, M. Levin, A. Shlayer and C. Estournès, Sintering and densification of nanocrystalline ceramic oxide powders: A review, *Advances in Applied Ceramics*, **27** 159, **2008**.

[21] F. Maglia, I. G. Tredici and U. Anselmi-Tamburini, Densification and properties of bulk nanocrystalline functional ceramics with grain size below 50 nm, *J. Eur. Ceram. Soc***., 33,** 1045, **2013**.

[22] R. Orrù, R. Licheri, A. M. Locci, A. Cincotti and G. Cao, Consolidation/synthesis of materials by electric current activated/assisted sintering. *Mat. Sc. and Eng Reports*, **63**, 127, **2009**.

[23] F. Caruso, Nanoengineering of particles, *Adv. Mater*., **13**, 11, **2011**.

[24] S. Mornet, C. Elissalde, V. Hornebecq, O. Bidault, E. Duguet, A. Brisson and M. Maglione, Controlled growth of silica shell on $Ba_{0.6}Sr_{0.4}TiO_3$ nanoparticles used as precursors of ferroelectric composites, *Chem. Mater*. **17**, 4530, **2005**.

[25] U.-C. Chung, C. Elissalde, F. Mompiou, J. Majimel, S. Gomez, C. Estournès, S. Marinel, A. Klein, F. Weill, D. Michau, S. Mornet and M. Maglione, Interface investigation in nanostructured $BaTiO_3$/silica composite ceramics, *J. Am. Ceram. Soc*. **93**, 865, **2010**.

[26] M. Legallais, S. Fourcade, U-C. Chung, D. Michau, M. Maglione, F. Mauvy and C. Elissalde, Fast re-oxidation kinetics and conduction pathway in Spark Plasma Sintered ferroelectric ceramics, *J. Eur. Ceram. Soc.* **38**, 543, **2018**.

[27] D. Nuzhnyy, P. Vaněk, J. Petzelt, V. Bovtun, M. Kempa, I. Gregora, M. Savinov, R. Krupková, V. Studnička, J. Buršík, M. I. Samoylovich and W. Schranz, Properties of $BaTiO_3$ confined in nanoporous Vycor and artificial opal silica, *Proc. Appl. Ceram.*, **4**, 215, **2010**.

[28] D. Nuzhnyy, J. Petzelt, I. Rychetsky, V. Buscaglia, M.T. Buscaglia and P. Nanni, THz and IR dielectric response of $BaTiO_3$ core–shell composites: evidence for interdiffusion, *J. Phys. D: Appl.Phys*. **42**, 155408, **2009**.

[29]. D. Nuzhnyy, J. Petzelt, V. Bovtun, M. Kempa, M. Svinov, C. Elissalde, U.C. Chung, D. Michau, C. Estournès and M. Maglione, High-frequency dielectric spectroscopy of $BaTiO_3$ Core–silica shell nanocomposites: Problem of interdiffusion, J. Adv. Diel. **1**, 309, **2011**.

[30] H. Han, C. Voisin. S. Guillemet-Fritsch, P. Dufour, C. Tenailleau, C. Turner and J. C. Nino, Origin of colossal permittivity in $BaTiO_3$ via broadband dielectric spectroscopy, *J. Appl. Phys*. **113**, 024102-1, **2013**.

[31] C. C. Homes, T. Vogt, S. M. Shapiro, S. Wakimoto and A. P. Ramirez, Optical Response of High-Dielectric-Constant Perovskite-Related Oxide, *Science,* **293**, 673, **2001**.

[32] J. Li, F. Li, C. Li, G. Yang, Z. Xu and S. Zhang: Evidence of grain boundary capacitance effect on the colossal dielectric permittivity in (Nb+In) co-doped TiO_2 ceramics, *Scient. Rep.* **5**, 8295-1, **2015**.

[33] D. A. Crandles, S. M. M. Yee, M. Savinov, D. Nuzhnyy, J. Petzelt, S. Kamba, and J. Prokes, Electrode effects in dielectric spectroscopy measurements on (Nb+In) co-doped TiO_2, J. Appl. Phys. **119**, 154105, **2016**.

[34] J. Petzelt, I. Rychetsky and D. Nuzhnyy: Dynamic ferroelectric-like softening due to the conduction in disordered and inhomogeneous systems: Giant permittivity phenomena, *Ferroelectrics* **526**, 171, **2012**.

[35] D. Nuzhnyy, E. Buixaderas, I. Rychetsky, C. Kadlec, J. Petzelt, H. Uršič, B. Malič: Percolation in the dielectric function of $Pb(Zr,Ti)O_3 – Pb_2Ru_2O_{6.5}$ ferroelectric – metal composites. *J. Phys. D: Appl. Phys.* **47**, 495301-1/6 (2014)

[36] M. Anoufa, J. M. Kiat, I. Kornev, and C. Bogicevic, Energy harvesting in core-shell ferroelectric ceramics: Theoretical approach and practical conclusions, *J. Appl. Phys*., **113**, 054104, **2013**.

[37] M. Anoufa, J. M. Kiat and C. Bogicevic, Electrocaloric effect in core-shell ferroelectric ceramics: Theoretical approach and practical conclusions, *Appl. Phys. Lett.*, **107**, 172902, **2015**.

[38] J. M. Kiat, B. Hehlen, M. Anoufa, C. Bogicevic, C. Curfs, B. Boyer, M. Al-Sabbagh, F. Porcher, and A. Al-Zein, Lowering of ground state induced by core-shell structure in strontium titanate, *Phys. Rev. B*, **93**, 144117, **2016**.

[39] U.-C. Chung, C. Elissalde, C. Estournès and M. Maglione, Controlling internal barrier in low loss $BaTiO_3$ supercapacitors, *Appl. Phys. Lett.*, **94**, 072903, **2009**.

[40] A. Artemenko, C. Elissalde, U.-C. Chung, C. Estournès, S. Mornet, I. Bykov and M. Maglione, Linking hopping conductivity to giant dielectric permittivity in oxides, *Appl. Phys. Lett*., **97**, 132901, **2010**.

[41] V.V. Laguta, A.M. Slipenyuk, I.P. Bykov, M.D. Glinchuk, M. Maglione, D. Michau, J. Rosa and L. Jastrabik, Electron Spin Resonance investigation of oxygen-vacancy related defects in $BaTiO_3$ thin films., *J. Appl. Phys.Lett*., **87**, 022903, **2005**.

[42] C. Elissalde, U.C. Chung, A. Artemenko, C. Estournès, R. Costes, M. Paté, J.P. Ganne, S. Wäechter and M. Maglione, Stoichiometry and grain boundaries control by Spark Plasma Sintering in $Ba_{0.6}Sr_{0.4}TiO_3$:Mn / MgO composites, *J. Am. Ceram. Soc*., **95**, 3239, **2012**.

[43] R. Berthelot, B. Basly, S. Buffiere, J. Majimel, G. Chevallier, A. Weibel, A. Veillere, L. Etienne, U-C. Chung, G. Goglio, M. Maglione, C. Estournes, S. Mornet and C. Elissalde, From Core-Shell $BaTiO_3$@MgO to Nanostructured Low Dielectric Loss Ceramics by Spark Plasma Sintering, *J. Mater. Chem*, **2**, 683, **2014.**

[44] R. Chaim, R. Marder, C. Estournes and Z. Shen, Spark and plasma in spark plasma sintering of rigid ceramic nanoparticles: A model system of YAG, *Adv. Appl. Ceram*., **35,** 111, **2012**.

[45] C. Aymonier, G. Philippot, A. Erriguible and S. Marre, Playing with solvents in supercritical conditions and the associated technologies for advanced materials by design, J. Supercrit. Fluids, **2018**, DOI: 10.1016/j.supflu.2017.12.021.

[46] S. Marre, A. Erriguible, A. Perdomo, F. Cansell, F. Marias, C. Aymonier, Kinetically-controlled formation of supported nanoparticles in low temperature supercritical media for the development of advanced nanostructured materials, *J. Phys. Chem. C*, , **113**, 5096, **2009**.

[47] J.A. Darr, J. Zhang, N.M. Makwana and X. Weng, Continuous hydrothermal synthesis of inorganic nanoparticles, *Chem. Rev.*, **117,** 11125, **2017**.

[48] G. Philippot, M. Albino, R. Ephere, G. Chevalier, A. Weibel, A. Peigney, M. Deluca, C. Elissalde, M. Maglione, C. Aymonier and C. Estournes, Local distortions in nanostructured ferroelectric ceramics through strain tuning, *Adv. Electron. Mater*., **1**, 1500190, **2015**.

[49] B. Giroire, S. Marre, A. Garcia, T. Cardinal and C. Aymonier, Continuous supercritical approach for quantum-confined GaN nanoparticles, *React. Chem. Eng*., **1**, 151, **2016**.

[50] M. Théodet, C. Quilfen, C. Martinez and C. Aymonier, Continuous supercritical synthesis of unsupported and high specific surface area catalyst precursors for deep-hydrodesulfurization, *J. Supercrit. Fluids*, **117**, 252, **2016**.

[51] C. Slostowski, S. Marre, P. Dagault, O. Babot, T. Toupance and C. Aymonier, CeO_2 nanopowders as solid sorbent for efficient CO_2 capture/release processes, *J. CO_2 Utilization*, **20,** 52**, 2017**.

[52] A. Dumas, M. Claverie, C. Slostowski, C. Le Roux, P. Micoud, F. Martin and C. Aymonier, Fast geomimicking using chemistry in supercritical water, *Angew. Chem. Int. Ed.*, **55,** 9795, **2016**.

[53] M. Majimel, S. Marre, E. Garrido and C. Aymonier, Supercritical Fluid Chemical Deposition as an alternative process to CVD for the surface modification of materials, *Chem. Vap. Deposition*, **17,** 342, **2011**.

[54] C. Erkey, Preparation of metallic supported nanoparticles and films using supercritical fluid deposition, *J. Supercrit. Fluids*, **47,** 517, **2009**.

[55] C. Aymonier, C. Elissalde, H. Reveron, F. Weill, M. Maglione and F. Cansell, Supercritical fluid technology of nanoparticles coating for new ceramic materials, J. Nanosci. Nanotech., **2005**, 5(6), 980-983.

[56] U. Anselmi-Tamburini, S. Gennari, J.E. Garay and Z.A. Munir, Fundamental investigations on the spark plasma sintering/synthesis process II. Modeling of current and temperature distributions, Materials *Science and Engineering A*, **394**, 139, **2005**.

[57] C. Manière, A. Pavia, L. Durand, G. Chevallier, K. Afanga and C. Estournès, *Finite-element modeling of the electro-thermal contacts in the spark plasma sintering process*, J. Eur. Ceram. Soc. **36**, 741, **2016**.

[58] J.A. Basmajian and R. C. Devries, Phase Equilibria in the System $BaTiO_3$–$SrTiO_3$, *J. Am. Ceram. Soc.*, **40**, 373, **1957.**

[59]. C.-W. Nan, M. I. Bichurin, S. Dong, D. Viehland and G. Srinivasan, Multiferroic magnetoelectric composites: Historical perspective, status, and future directions, *J. Appl. Phys.*, **103**, 031101, **2008**.

[60]. L. W. Martin, S. P. Crane, Y.-H. Chu, M. B. Holcomb, M. Gajek, M. Huijben, C.-H. Yang, N. Balke and R. Ramesh, Multiferroics and magnetoelectrics: thin films and nanostructures, *J. Phys.: Condens. Matter*, **20**, 434220, **2008**.

[61]. G. Schileo, Recent developments in ceramic multiferroic composites based on core/shell and other heterostructures obtained by sol–gel routes, *Prog. Solid State Chem.*, **41**, 87, **2013**.

[62]. N. Spaldin and M. Fiebig, The renaissance of magnetoelectric multiferroics, *Science*, **309**, 391, **2005**.

[63]. W. Eerenstein, N. D. Mathur and J. F. Scott, Multiferroic and magnetoelectric materials, *Nature*, , **442**, 759, **2006**.

[64]. A. M. J. G. Van Run, D. R. Terrell and J. H. Scholing, An *in situ* grown eutectic magnetoelectric composite material, *J. Mater. Sci.*, **9**, 1710, **1974**.

[65]. R. A. Islam and S. Priya, ME response of cofired trilayer magnetoelectric composites with partial texturing, *J. Mater. Sci.*, , **44**, 5935, **2009**.

[66]. J. Ryu, S. Priya, K. Uchino and H. E. Kim, Magnetoelectric effect in composites of magnetostrictive and piezoelectric materials, *J. Electroceram.*, **8**, 107, **2012**.

[67]. K. Mori and M. Wuttig, Magnetoelectric coupling in Terfenol-D/polyvinylidenedifluoride composites, *Appl. Phys. Lett.*, **81**, 100, **2002**.

[68]. H. Zheng, J. Wang, S. E. Lofland, Z. Ma, L. Mohaddes-Ardabili, T. Zhao, L. Salamanca-Riba, S. R. Shinde, S. B. Ogale, F. Bai, D. Viehland, Y. Jia, D. G. Schlom, M. Wuttig, A. Roytburd and R. Ramesh, Multiferroic $BaTiO_3$-$CoFe_2O_4$ nanostructures, *Science*, **303**, 661, **2004**.

[69]. F. Zavaliche, H. Zheng, L. Mohaddes-Ardabili S. Y. Yang, Q. Zhan, P. Shafer, E. Reilly, R. Chopdekar, Y. Jia, P. Wright, D. G. Schlom, Y. Suzuki and R. Ramesh, Electric field-induced magnetization switching in epitaxial columnar nanostructures, Nano Lett., **5**, 1793, **2005**.

[70]. F. Yao, L. Xu, B. Lin and G.-D. Fu, Preparation and applications of functional nanofibers based on the combination of electrospinning, controlled radical polymerization and 'Click Chemistry', *Nanoscale*, **2**, 1348, **2010**.

[71]. S. Xie, F. Ma, Y. Liu and J. Li, Multiferroic $CoFe_2O_4$–$Pb(Zr_{0.52}Ti_{0.48})O_3$ core-shell nanofibers and their magnetoelectric coupling, *Nanoscale*, **3**, 3152, **2011**.

[72] S. Mornet, C. Elissalde, O. Bidault, F. Weill, E. Sellier, O. Nguyen and M. Maglione, Ferroelectric-based nanocomposites: towards multifunctional materials. *Chem. Mater.* **19**, 987, **2007.**

[73] J. S. Andrew, J. D. Starr, M. A. K. Budi, Prospects for nanostructured multiferroic composite materials, *Scr. Mater.*, **74**, 38, **2014**.

[74] M. Liu, X. Li, H. Imrane, Y. Chen, T. Goodrich, Z. Cai, K. S. Ziemer, J. Y. Huang, N. X. Sun, Synthesis of ordered arrays of multiferroic $NiFe_2O_4$-$Pb(Zr_{0.52}Ti_{0.48})O_3$ core-shell nanowires, *Appl. Phys. Lett.*, **90**, 152501, **2007**.

[75] T. N. Narayanan, B. P. Mandal, A. K. Tyagi, A. Kumarasiri, X. Zhan, M. G. Hahm, M. R. Anantharaman, G. Lawes, P. M. Ajayan, Hybrid multiferroic nanostructure with magnetic–dielectric coupling, *Nano Lett.*,12, 3025, **2012.**

[76] D. Sallagoity, C. Elissalde, J. Majimel, R. Berthelot, U. C. Chung, N. Penin, M. Maglione, V. A. Antohe, G. Hamoir, F. Abreu Araujo and L. Piraux, Synthesis and magnetic properties of Ni–$BaTiO_3$ nanocable arrays within ordered anodic alumina templates, *J. Mater. Chem. C*, **3**, 107, **2015**.

[77] B. D. Cullity, C. D. Graham, *Introduction to magnetic materials.* 2nd edn., Hanzo, L. ed. (Hoboken, NJ: A John Wiley & Sons, Inc.), pp 141-183, **2009**.

[78] Z. Hua, P. Yang, H. Huang, J. Wan, Z.-Z. Yu, S. Yang, M. Lu, B. Gu and Y. Du, Sol–gel template synthesis and characterization of magnetoelectric $CoFe_2O_4$/$Pb(Zr_{0.52}Ti_{0.48})O_3$ nanotubes, *Mater. Chem. Phys.*, **107**, 541, **2008**.

[79] D. Tang, Z. Zeng, Q. Zhou, S. Su, D. Hu, P. Li, X. Lin, X. Gao, X. Lu, X. Wang, M. Jin, G. Zhou, Z. Zhang and J. Liu, Ordered multiferroic $CoFe_2O_4$–$Pb(Zr_{0.52}Ti_{0.48})O_3$ coaxial nanotube arrays with enhanced magnetoelectric coupling *RSC Adv*., **7**, 29096, **2017**.

[80] B. Fu, R. Lu, K. Gao, Y. Yang and Y. Wang, Substrate clamping effect onto magnetoelectric coupling in multiferroic $BaTiO_3$-$CoFe_2O_4$ core-shell nanofibers via coaxial electrospinning, *EPL*, **112**, 27002, **2015**.

[81] G. Sreenivasulu, J. Zhang, R. Zhang, M. Popov, V. Petrov and G. Srinivasan, Multiferroic core-shell nanofibers, assembly in a magnetic field, and studies on magneto-electric interactions, *Materials*, **11**, 18, **2018**.

[82] T. M. Shaw and S. Trolier-McKinstry, The Properties of Ferroelectric Films at Small Dimensions, *Ann. Rev. Mater. Sci.*, **30**, 263, **2000.**

[83] J. Junquera and P. Ghosez, Critical thickness for ferroelectricity in perovskite ultrathin films, *Nature*, **422**, 506, **2003**.

[84] C. H. Ahn, K. M. Rabe and J.-M. Triscone, Ferroelectricity at the nanoscale: local polarization in oxide thin films and heterostructures, *Science*, **303**, 488, **2004**.

[85] A. Encinas-Oropesa, M. Demand, L. Piraux, I. Huynen and U. Ebels, Dipolar interactions in arrays of nickel nanowires studied by ferromagnetic resonance, *Phys. Rev.* B, **63**, 104415, **2001**.

[86] D. Sallagoity, C. Elissalde, J. Majimel, M. Maglione, V. A. Antohe, F. A. Araujo, P. M. Pereira de Sá, S. Basov and L. Piraux Synthesis of dense arrays of multiferroic $CoFe_2O_4$–$PbZr_{0.52}Ti_{0.48}O_3$ core/shell nanocables, *RSC Adv.*, **6**, 106716, **2016**.

[87]. J. Kim, S. A. Yang, Y. C. Choi, J. K. Han, K. O. Jeong, Y. J. Yun, D. J. Kim, S. M. Yang, D. Yoon, H. Cheong, K.-S. Chang, T. W. Noh and S. D. Bu, Ferroelectricity in highly ordered arrays of ultra-thin-walled $Pb(Zr,Ti)O_3$ nanotubes composed of nanometer-sized perovskite crystallites, *Nano Lett.*, **8**, 1813, **2008**.

[88]. A. Gruverman, O. Auciello and H. Tokumoto, Imaging and control of domain structures in ferroelectric thin films via scanning force microscopy, *Annu. Rev. Mater. Sci.*, **28**, 101, **1998**.